Composite Structures 320 (2023) 117215

Contents lists available at ScienceDirect

Composite Structures

journal homepage: www.elsevier.com/locate/compstruct

Data driven statistical method for the multiscale characterization and modelling of fiber reinforced composites

A Ciampaglia

Politecnico di Torino, Department of Mechanical and Aerospace Engineering, Torino, Italy

ARTICLE INFO

Keywords:
Statistical methods
Glass fibres
Micro-mechanics
Tomography
Stochastic volume element

ABSTRACT

Multiscale analysis of composite laminates allows for predicting the mechanical response of these materials avoiding cumbersome experimental campaigns. The matrix and fibre material properties and the size of the Representative Volume Element (RVE) are the main parameters affecting the accuracy of multiscale models. This paper proposes a statistical inverse method to calibrate micromechanical material parameters from macroscale experiments and 3D reconstruction. First, glass fiber reinforced epoxy laminates have been analysed with Computer Tomography (CT), then, the material 3D microstructure has been reconstructed and fibre, matrix, and voids were segmented. Tensile tests have been performed on the composite specimen, measuring the surface strains with a Digital Image Correlation (DIC) system. The reconstructed volume, converted to a voxel mesh, has been used to compute the homogenized response of composite by Fast Fourier Transform (FFT) analysis. By comparing the marginal distribution of homogenized material stiffness extracted from DIC data of tensile tests, with the conditioned distribution computed by varying the FFT model parameter, a Stochastic Volume Element (SVE) is finally calibrated. A probabilistic multiscale model based on the SVE that propagates the uncertainty from the microscale to the structure level is presented.

1. Introduction

Polymer matrix composites (PMC) reinforced with continuous fibres play an established role in the design of aerospace structures, and their application is now spreading to diverse industrial sectors such as automotive [1-11] and wind energy [12-14]. The increasing interest in PMC is pushing the adoption of novel reinforcement and matrices, widening the composite material portfolio available to structural designers. Predicting the mechanical response of new composite materials with a conventional approach requires extensive experimental campaigns, which may result in unpracticable. This has led to the spread of multiscale models that can predict the response of any composite materials by individually modelling the matrix and fibres [15-21].

Multiscale models compute the local response of composite introducing a Representative Volume Element (RVE) [22], a lower scale inhomogeneous representation of the composite material, whose response is homogenized and transferred to the higher scale model. RVEs are defined as the smallest volume over which a measurement can be made that yields a value representative of the whole.

Conventional approaches assume a deterministic description of the micromechanical properties (e.g., microstructure, matrix properties, fibre properties), but there is an inevitable need to establish multiscale statistical microstructure–constitutive property relations in materials design. Researchers have proposed effective methods to account for the stochastic nature of the composite microstructure, by defining statistical descriptors of random microstructures [23-25] that could be experimentally characterized with microstructural images or CT reconstructions [26-30]. [30] introduced the concept of Stochastic Volume Element (SVE), a statistically equivalent volume element introduced to account for the randomness of material microstructure on the composite constitutive properties. [31-34] proposed a statistical multiscale method to propagate the microstructural uncertainty to the structural level by introducing a statistical representation of the RVE. Recently, [35] proposed a probabilistic micromechanical-based approach to account for the effect of scattering sources in composite materials, focusing on voids, material inhomogeneity, fibre morphology, and other manufacturing-induced defects.

The mentioned studies assume that the scatter in the mechanical response of composite materials is imputable to the microstructure variation. However, [36-38] provided evidence that the in-situ elastic modulus of the epoxy matrix within the composite spatially varies within the material, contributing to the scatter of the homogenized

E-mail address: alberto.ciampaglia@polito.it.

https://doi.org/10.1016/j.compstruct.2023.117215
Received 15 December 2022; Received in revised form 30 May 2023; Accepted 31 May 2023
Available online 7 June 2023

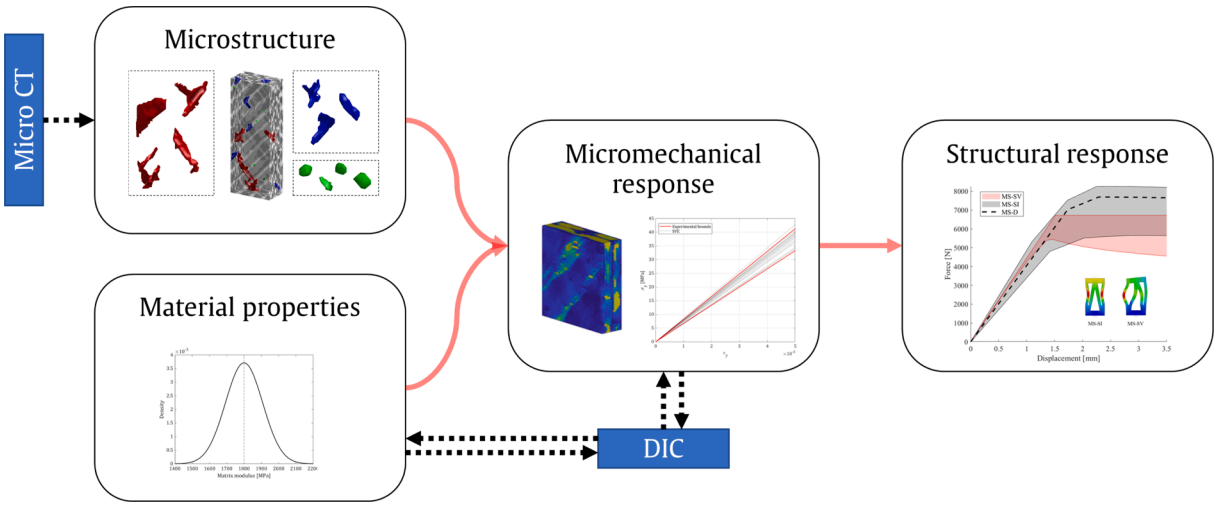

Fig. 1. Multiscale framework calibrated on experimental data to model the uncertainty in composite structures.

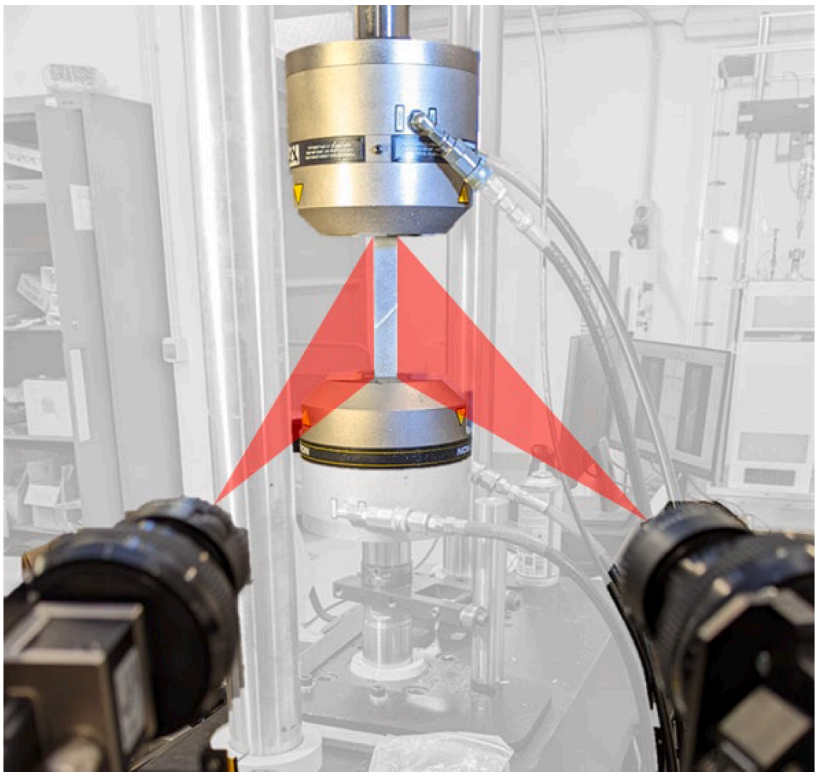

Fig. 2. Experimental setup of the tensile test recorded with a stereo camera system for 3D Digital Image Correlation.

Table 1
VGDefX algorithm parameters for void segmentation.

Parameter	Value
Min. Volume [vox.]	1000
Max. Diameter [vox]	3000
Voxel count	0.3
Compactness	0.5
Scaled deviation	0.5
Ignore small defect	0.7
Sphericity	0.3

response. The microscale mechanism governing the variation of the elastic response of thermoset polymers has been experimentally investigated with atomic force microscopy (AFM) analysis [39] which revealed a 30% variation of the modulus with the curing state of the polymer. Furthermore, to the author's best knowledge, only a few studies in the literature describe an experimental procedure to determine the RVE size [40,41] and its statistical description from mechanical tests.

The scope of this work is:

- Extending the current methodologies by introducing a statistical representation of the in-situ matrix properties in the representative volume at the mesoscale level.

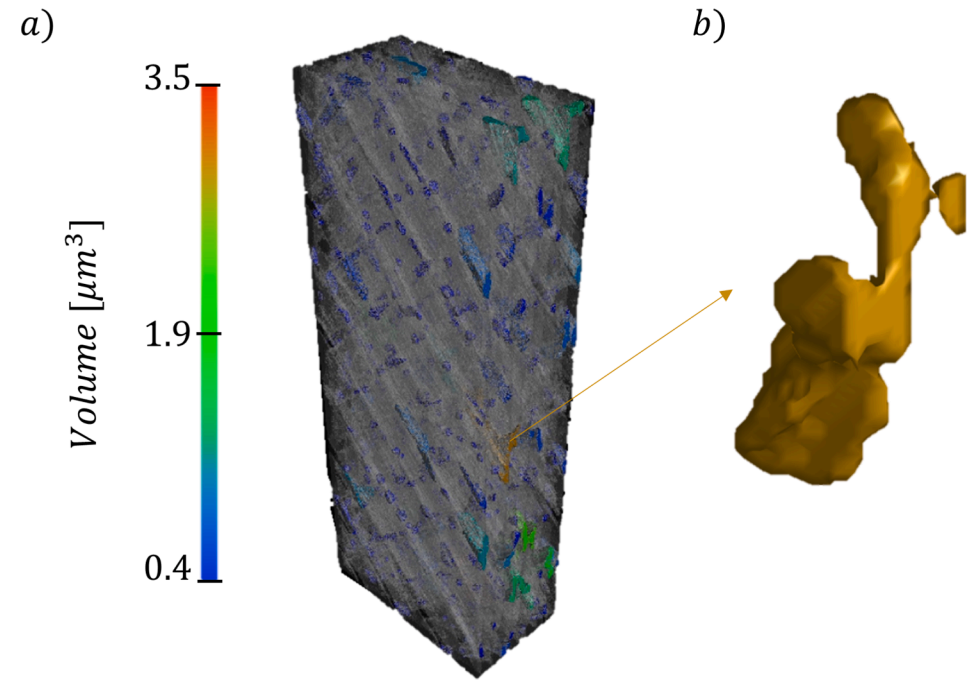

Fig. 3. a) VGDefX results of a porosity analysis on a composite specimen b) a pore in the composite material.

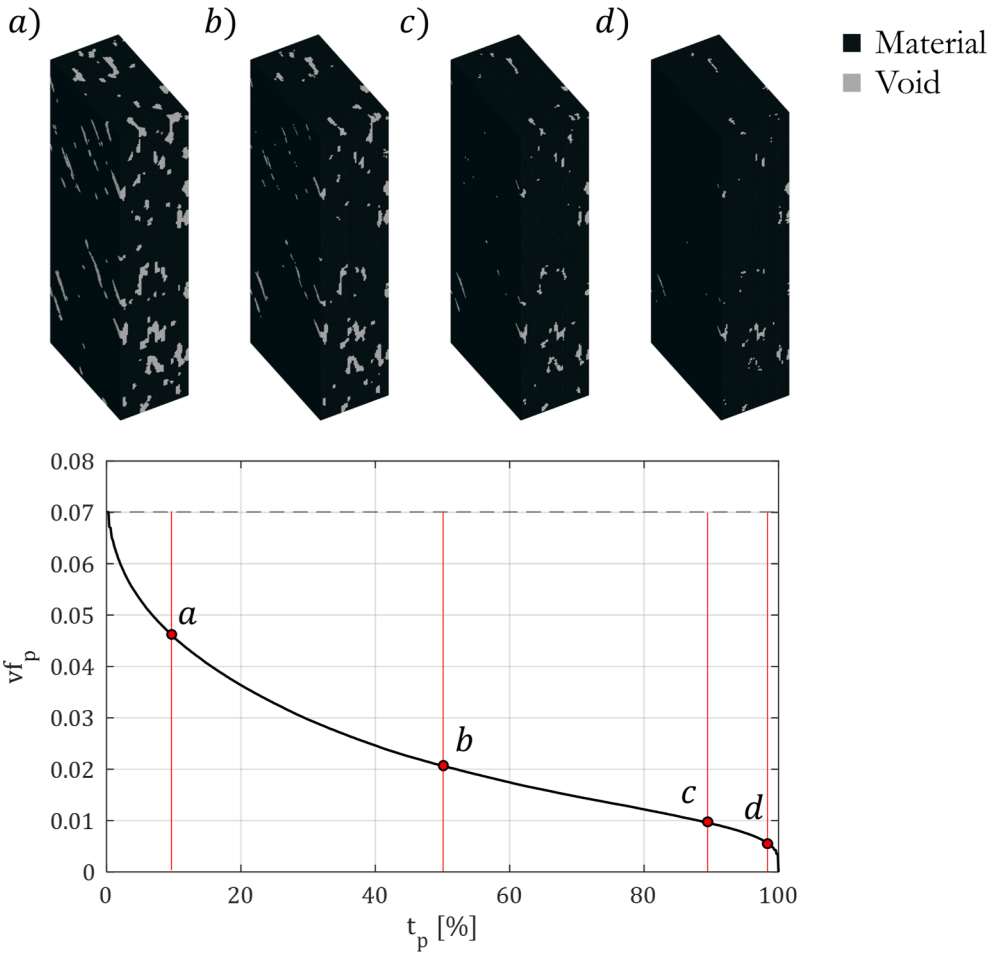

Fig. 4. On the top the binarized porosity maps with a threshold of a) 10%, b) 50%, c) 90%, d) 99%. On the bottom, the variation of the porosity with the threshold value is expressed as a volume fraction.

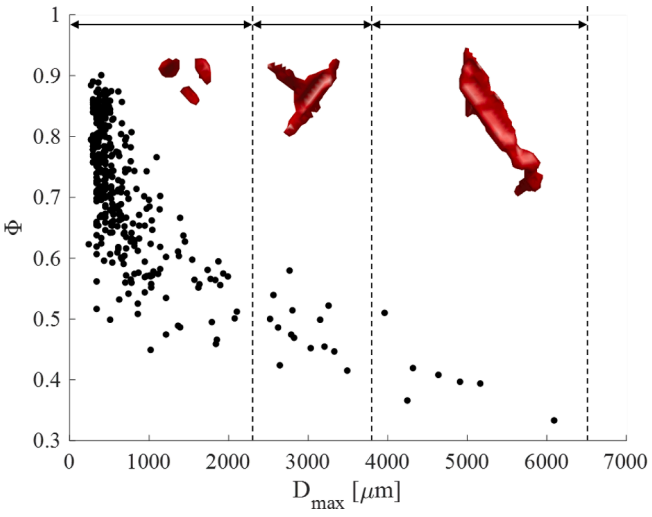

Fig. 5. Sphericity computer for all the clustered defects against its main diameter. Representative defects of each interval are reported.

- Introducing a novel approach to calibrate the SVE size (extending the study in [40]) from Digital Image Correlation Data of tensile tests.
- Presenting a novel procedure to calibrate stochastic properties of the extended SVE with experimental results from the tensile test and micro-CT reconstruction.

The presented work introduces a general probabilistic framework for the multiscale modelling of composite structures, calibrated on experimental data (Fig. 1).

The novelty of the proposed methodology relies on the combination of multiscale modelling and experimental characterization methods to capture the variation in the elastic response of the composite at the mesoscale.

2. Materials and methods

2.1. Materials

The material under study is a glass fiber reinforced epoxy matrix manufactured by hand lay-up. The matrix is the low viscosity (70 mPas) epoxy resin AXSON EPOLAM 2015 with a glass temperature of 90°, mixed with the EPOLAM hardener at 32% of weight fraction. The unidirectional E-glass fabric UNIE600 (ResinTex) has a surface weight of 661 g/m^2 and a total tex of 2400. The fibre diameter spans from 14 to 17 μm with a density of 2.60 g/cm^3 and a nominal elastic modulus of 73 GPa. Laminates are produced in the shape of 300x300 mm plates and successively shaped to get rectangular specimens with a Wazer waterjet cutting machine. The laminates had a $[\pm 45]_6$ stacking sequence, with 12 layers in total, each with a nominal thickness of 0.7 mm, yielding a total laminate thickness of 8.55 ± 0.10 mm. Rectangular specimens are cut with a 25 mm width and a length of 250 mm each and visually inspected to ensure that the cutting process has not induced any damage or delamination to the specimen.

2.2. Experiments

2.2.1. Computer tomography analysis

Specimens have been scanned with the Fraunhofer IKTS Computer Tomography scan available in Politecnico Labs with an open microfocus x-ray tube operating at a maximum voltage of 300 kV. The X-Ray detector has a size of 400 × 400 mm with 2048x2048 pixels (200 μm resolution). The X-ray image resolution was 5 μm under the most favourable conditions (i.e., sample size, scanning speed, sample shape). The object-to-detector distance and source-to-detector distance were set to 50 mm and 545 mm, respectively, yielding a voxel-edge resolution of 16 μm. The specimen has been placed with its main direction aligned to the rotation axis and scanned four times in each of the 1600 projection positions. The tube voltage and filament current have been set to 100 kV and 60 μA, respectively. To increase the accuracy of the X-ray images, an aluminium filter of thickness 0.2 mm has been used to cut out low-intensity rays.

2.2.2. Tensile test and Digital Image Correlation

Tensile specimens had a width of 25 mm and a total length between the grips of 150 mm, as suggested by the ASTM standards D3039. The test has been performed with the servo-hydraulic testing machine 8801 by Instron, equipped with a load cell with a 100 kN capacity. Specimens have been clamped with a hydraulic system, setting a closure pressure low enough to minimize the stress concentration at the interface. The test has been performed at a fixed displacement rate of the lower crosshead of 2 mm/min, with an acquisition frequency of 20 Hz for both load and displacement. The tensile tests were recorded with a high-

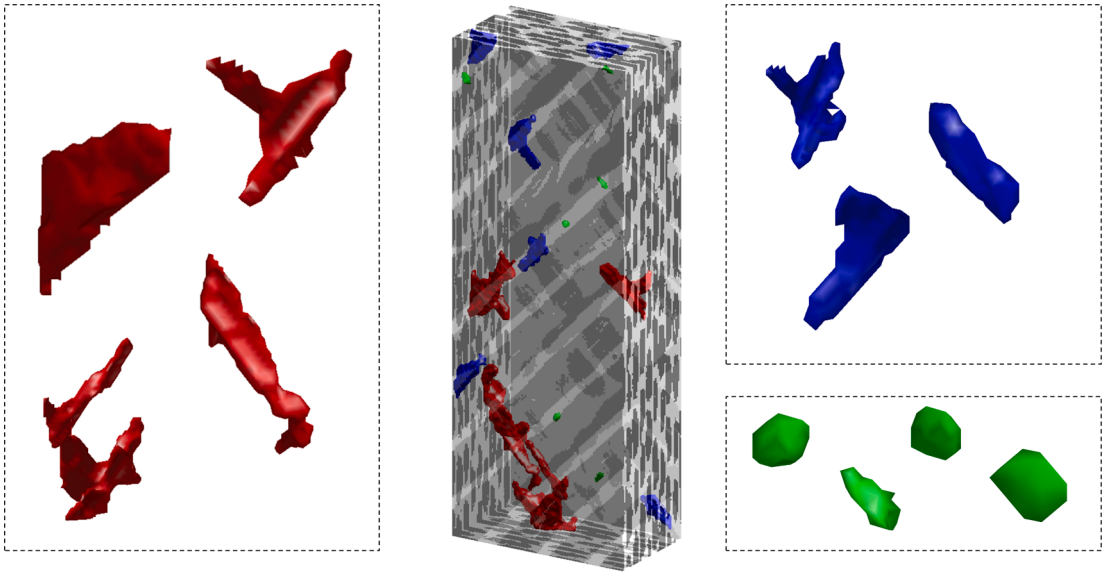

Fig. 6. Reconstructed mesh with main defects grouped by sphericity and dimension.

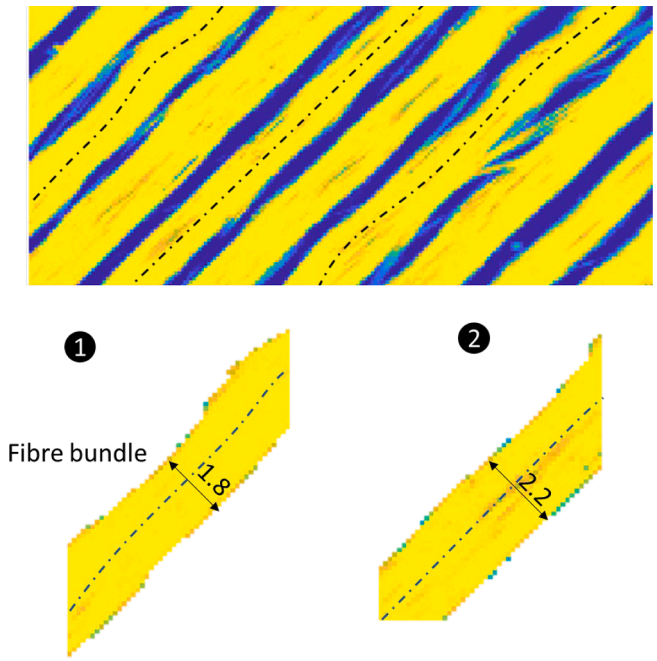

Fig. 7. A slice of the reconstructed mesoscale structure of the composite where the waviness of the bundles is indicated with a dot-dashed line. In the bottom, two segmented sections of the two tows with different diameters and waviness.

resolution stereo camera system by Isi Systems, with a 4096 by 2160 pixels resolution and an acquisition frequency of 5 Hz. The experimental setup is shown in Fig. 2. The cameras are controlled and calibrated with the VIC-3D software by Correlated Solutions, later used to compute surface displacements and strains on the specimen using the Digital Image Correlation (DIC) method.

2.3. Methods

This paper proposes an inverse statistical methodology to calibrate a Stochastic Volume Element (SVE) for multiscale analysis from a macroscale tensile test and micro-CT scan. From the micro-CT data, the mesoscale structure of the laminate has been subdivided through a segmentation of the volume voxels into matrix, void, and tows (as will be described in Section 3.1). From the segmented voxel volume, the extracted laminate sub-regions (i.e., candidate RVEs) are converted to voxel mesh and transferred to a Fast Fourier Transform solver developed in MATLAB (as it will be described in Section 3.2). Similarly to what has been done for the voxel mesh, surface sub-regions of the Digital Image Correlation maps with the same size have been designed and an average stiffness has been computed from synchronous strain and load data (as it will be described in Section 3.4). It is assumed that DIC measurements are descriptive of all the uncertain variables defining the material mechanical response, while the reconstructed CT-scan mesh is a deterministic description of the mesoscale geometry. On the base of these assumptions, the statistical distributions of the microscale material parameters have been optimized to best match the empirical distributions of the elastic modulus measured through DIC. To achieve these results, the cumulative distribution function (CDF) of the FFT results obtained by varying the material random variable has been compared with the DIC CDF. The loss function of the optimization scheme is defined as the p-value of the Kolmogorov-Smirnov [42] test, weighted on the test results (as it will be described in Section 3.5).

2.3.1. Data segmentation and mesh reconstruction

The X-ray image of the 1600 projections around the scanning axis has been imported into VGMax software to reconstruct a 3D volume of the specimen. The volume voxel-edge resolution is 16 μm, each voxel has a grey scale value between 0 and 255 that represents the absorbed power of the material in each position. Using a threshold algorithm on the greyscale distribution curve, materials have been differentiated from voids, assigning each voxel to one of these classes. Voids have been then processed with the VGDefX algorithm that clusters the void voxels and

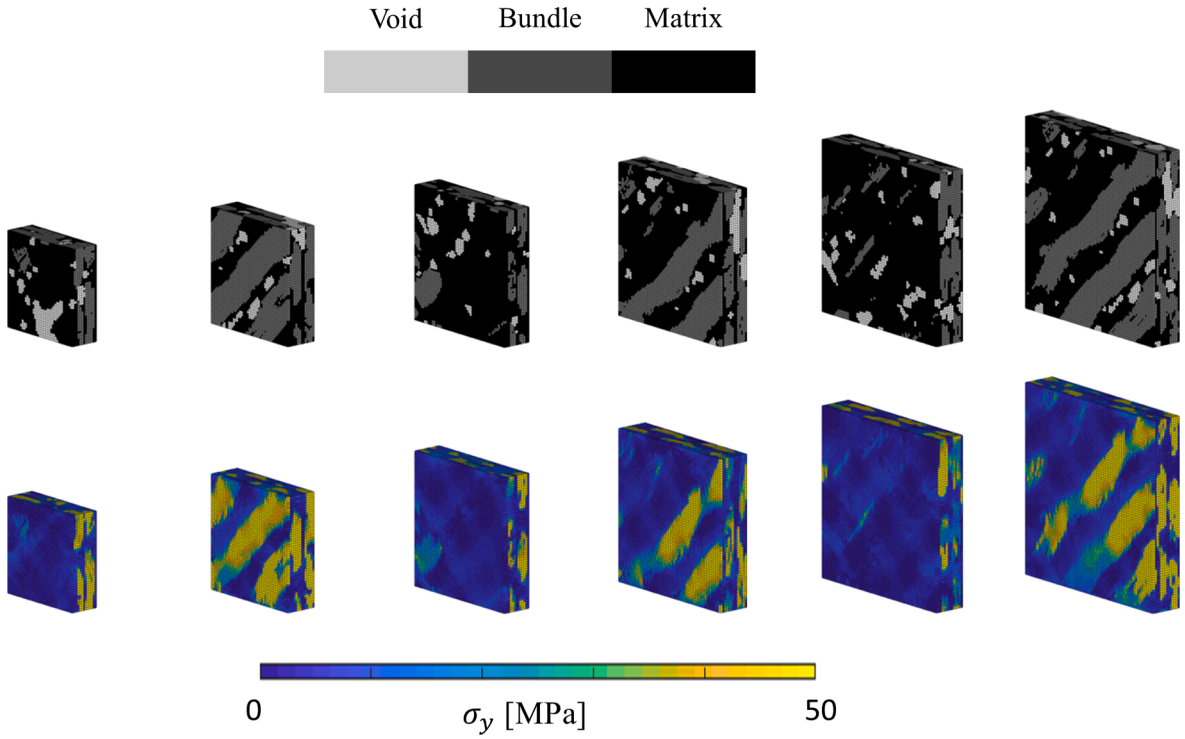

Fig. 8. A) microstructures of heterogeneous volume elements reconstructed from the ct images. b) longitudinal stress on the volume element when a uniaxial strain of 0.01 mm/mm is applied along the y direction. The RVE size is 4.5, 5.5, 7.5, 8.5, 10, and 11 mm, from left to right.

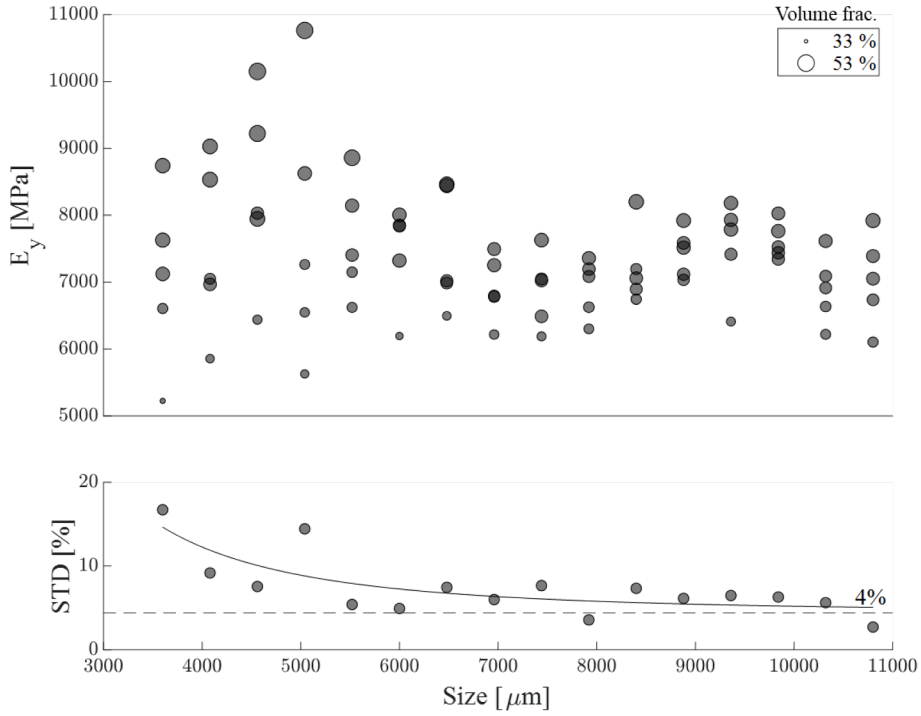

Fig. 9. Convergence study of the RVE size estimated from FFT analysis on CT reconstructed mesh.

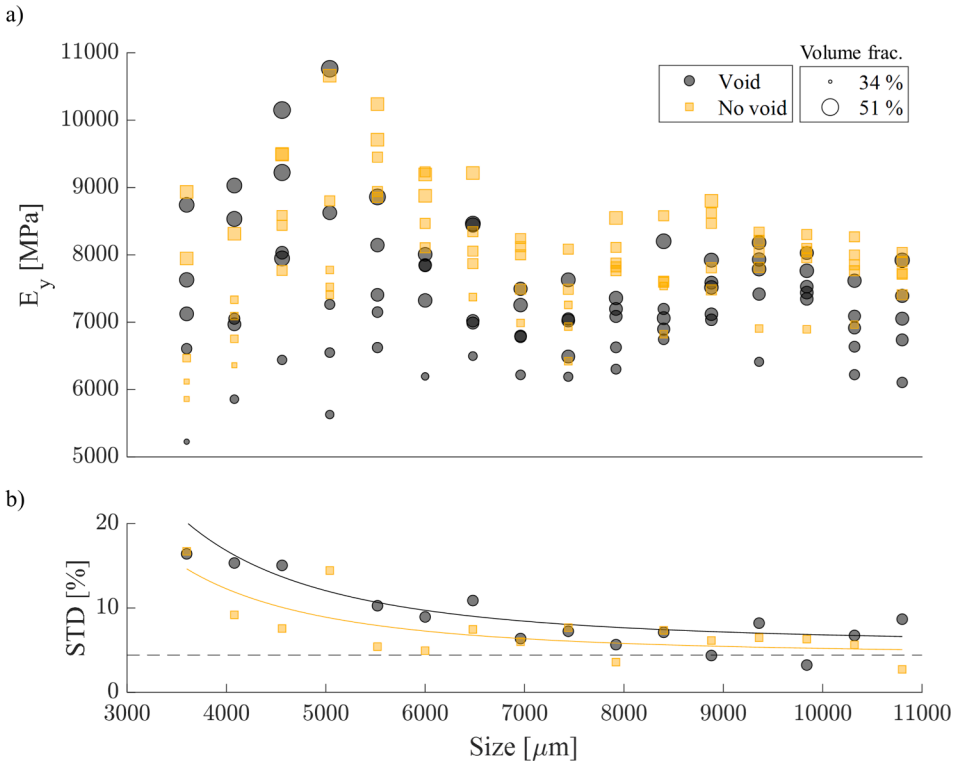

Fig. 10. On top, the homogenized modulus computed with FFT simulations of reconstructed microstructures, on the bottom, the standard deviation normalized to the mean.

estimates the probability (p_p) that a cluster is a porosity (i.e. a defect), rather than an artefact. The probability has been weighted on the geometrical features of the clusters.

Voxels labelled as "composite" are processed with the Fibre Composite tool by VGMax, which interpolates the grey values of the voxels and converts them to a volume fraction (v_f). The volume fraction of each voxel can be used to differentiate between matrix ($v_f = 0$) and fibre tows ($v_f \cong 1$). Since the resolution of the scan was twice the fibre diameter, the algorithm could not distinguish fibre and matrix within the tows, therefore the volume fraction computed with VGMax had to be carefully treated, being limited by the CT resolution. To overcome this issue, a microscopic image of the tow has been taken to properly assess the fibre

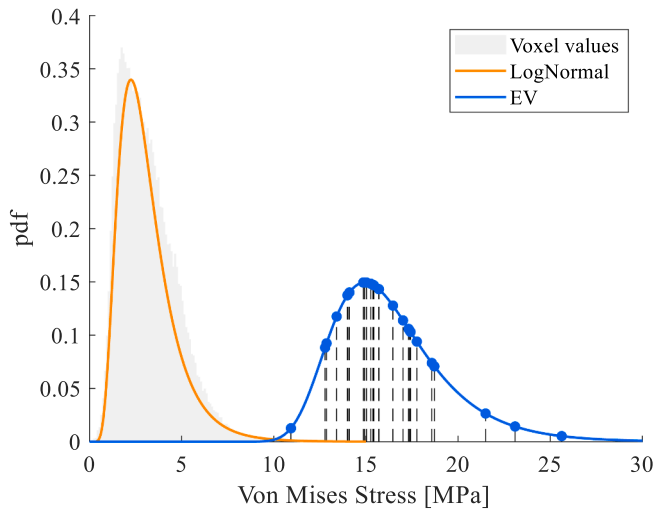

Fig. 11. The equivalent Von Mises stress computed at each matrix voxels of the FFT calculations computed over different RVEs. The histogram reports all the voxels values, while the orange line represents the logarithmic normal distribution fitted on the data. The dashed black lines and filled blue dots indicate the maximum Von Mises stress at each simulation, while the blue line shows the extreme values distribution fitted on the maximum stresses. (For interpretation of the references to colour in this figure legend, the reader is referred to the web version of this article.)

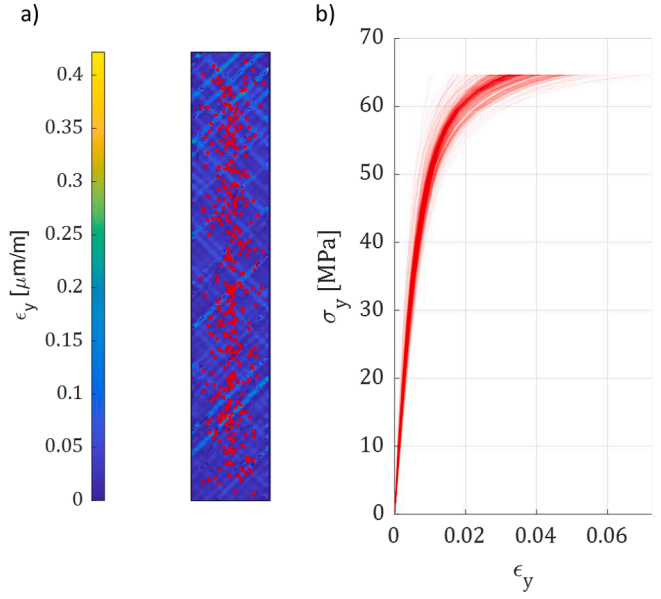

Fig. 12. A) centroid of the rve displayed on the strain maps at a nominal stress of 20 MPa. b)The homogenized stress–strain response of different RVE with different sizes extracted from the DIC map.

volume fraction within it.

The voxel discretized volume has been exported into a MATLAB environment in the form of vectors containing voxel class labels, porosity probability, volume fraction, and spatial coordinates.

The continuous variables v_f and p_p have been converted into discrete values by defining the threshold values:

- t_p: probability threshold, voxel with a porosity probability above t_p have been labelled as pore, the remaining voxels have been labelled as matrix
- t_v: volume fraction threshold, voxels with a computed volume fraction above t_v have been labelled as tows, and the remaining voxels have been labelled as matrix.

The resultant mesh has been later divided into different layers by manually defining the layers' interface positions along the thickness.

The reconstructed mesh has been used as the seed to generate Volume Elements (VEs) by extracting a sub-volume of the mesh with a random position in the plane and a fixed number of layers. The size of the in-plane square and the number of layers then define the size and aspect ratio of the extracted VE.

2.3.2. RVE size estimation from FFT on CT reconstruction

RVE is the smallest volume over which a measurement can be made that yields a value representative of the whole. The RVE size is commonly identified by computing the homogenized mechanical response (e.g., tensile stiffness) of the VEs with the increasing size until the quantity of interest is unchanged and its standard deviation is below a defined threshold [43]. Therefore, multiple VE with increasing size have been extracted and the homogenized in-plane shear modulus G_{12} has been computed with FFT simulations, until it converged to a stationary value.

2.3.3. RVE size estimation from DIC measurements

The DIC strain map resolution of 0.3 mm is approximately one-third the fibre tow width, yielding an inhomogeneous distribution of the surface strain. It is then possible to compute a homogenized strain value over a surface sub-region with Eq. (1):

$$\bar{\varepsilon} = \frac{1}{A}\int_{\Omega} \varepsilon(x,y)dS \tag{1}$$

where Ω is the surface sub-region with area A, and $\varepsilon(x,y)$ is the strain field computed with the DIC. The stress $\bar{\sigma}_y$ in every point is equal to the applied stress that can be measured by dividing the measured force over the cross-sectional area. On the specimen surface, the out-of-plane stress is null, thus a plane stress condition is assumed, which yields to Eq. (2):

$$E_y = \frac{(1-\nu)\bar{\sigma}_y}{\bar{\varepsilon}_x + \nu\bar{\varepsilon}_y} \tag{2}$$

The homogenized longitudinal modulus has been computed for sub-regions with increasing size, i.e. Surface Representative Volume Element (S-RVE). Similarly, the in-plane shear modulus G_{12} can be computed from Eq.(3).

$$G_{12} = \frac{\bar{\sigma}_y}{2\left(\bar{\varepsilon}_y - \bar{\varepsilon}_x\right)} \tag{3}$$

The RVE size has been defined by analysing the convergence of the homogenized moduli with the increasing area.

The proposed methodology underlies the fundamental assumption that the in-plane strain measured on the specimen surface is representative of the average strain through the thickness. Previous works [44,45] have investigated the stress concentration on the surface of the textile composites induced by the material microstructure. It has been assessed that an increase of the stress (or strain) in the woven composite is induced by the local unbalancing of the laminate determined by the woven architecture. The induced momentum can be computed as:

$$\frac{\Delta F}{F} = \left(\frac{1}{2} - \frac{t}{h}\right)\left(\frac{N}{N-1}\right) \tag{4}$$

where h is the ply thickness, and t is the distance from the unit cell surface and the yarn midline. In the case of the bundled unidirectional composite under study, t is half of the cell thickness, yielding a null induced momentum on the outer surface. It can be then concluded that in the case of the unidirectional composite under study, the surface stress is not altered by the material structure.

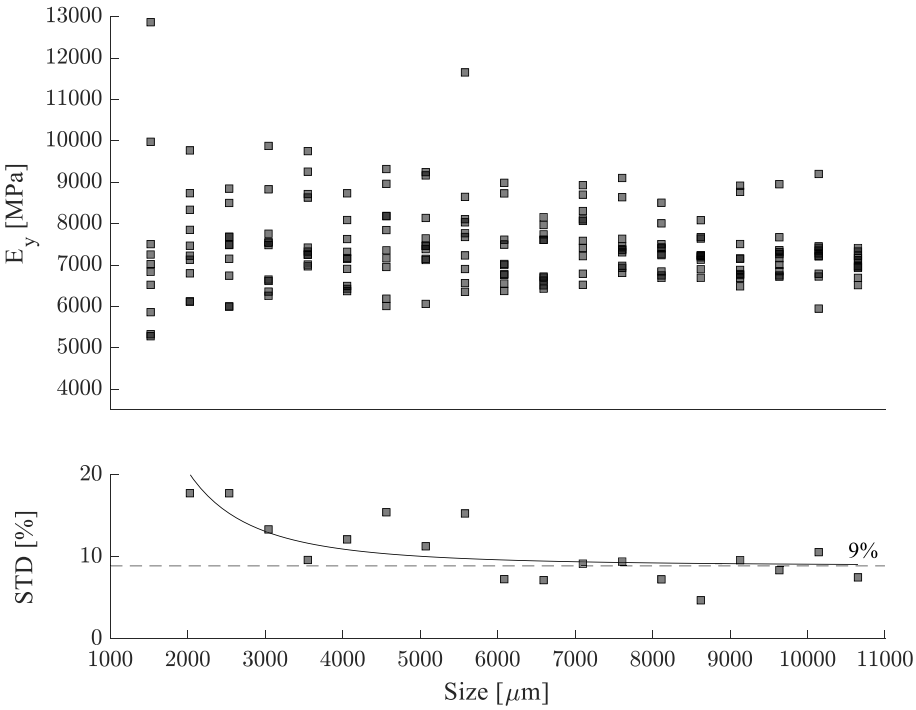

Fig. 13. Results of the RVE size analysis from the DIC measurements during the tensile test.

2.3.4. Stochastic volume Element (SVE) calibration

The mechanical response measured with tensile test and DIC is representative of the glass fibre material and intrinsically contains all the variance associated with porosities, variable local volume fraction, and variable matrix properties over the specimen volume. While the geometrical irregularities can be measured with the CT scans, the statistical distribution of the constituents' properties is unknown and a punctual measurement, e.g. with a nano-indenter, would require an extensive characterization campaign with additional characterization experiments. The objective of the proposed method is therefore to estimate the variation of the elastic response at the mesoscale, that is an average response of the nanoscale variations related to the crosslinking of the polymers governed by the curing kinematics[39]. This paper proposes an inverse method to calibrate the statistical distribution of the constituent properties by minimizing the difference between the CDFs of the homogenized properties drawn from the FFT simulations with variable matrix modulus and from the DIC measurements. The empirical CDF is inferred from the tensile test fitting the homogenized stiffness distribution obtained by repeating the procedure described in Section 2.3.4 with the computed RVE size. The CDF of the FFT model, F_E^{FFT}, can be estimated from the conditioned probability $F_{E|E_m}$ using Eq. (5):

$$F_E^{FFT} = \int F_{E|E_m} f_{E_m} dE_m \tag{5}$$

where $F_{E|E_m}$ is the conditional CDF of the homogenized modulus at a fixed Young's modulus of the matrix, E_m, and f_{E_m} is the probability function of E_m. $F_{E|E_m}$ is computed from the homogenized modulus of 10 RVE simulations, with different randomly selected locations in the scanned volume, with a fixed E_m. The conditional CDF has been computed at different E_m, sampled within 1 GPa and 4 GPa.

The distribution of the matrix modulus has been assumed to be Normal, with mean μ and standard deviation σ obtained with an optimization procedure. The adopted optimizer finds the μ and σ values that minimize the loss function in Eq. (6):

$$\mathscr{L} = 1 - pp(1 - hh), \tag{6}$$

where pp and hh are the p-values of the Kolmogorov-Smirnov test[42], and the test results at a significance level of 10%, respectively.

The test statistic is the maximum absolute value between the empirical cdf calculated from the DIC data and the hypothesized conditional CDF:

$$D^* = \max\left(\left|F_E^{DIC} - \int F_{E|E_m} f_{E_m}(\mu_{E_m}, \sigma_{E_m}) dE_m\right|\right) \tag{7}$$

The critical value for text acceptance is computed with the empirical formula described in [42].

The gradient-based optimization algorithm used for the calibration of the distribution of the matrix modulus is based on the interior-point approach to constrained minimization, able to solve optimization problems with inequality constraints. More details on the algorithm are given in [46].

3. Results

This section is organized as follows:

Section 3.1 presents the experimental results of the microstructure reconstruction from the CT scans and micrographic images.

Section 3.2 introduces the FFT model calibration, and the results compared to the tensile test.

In Section 3.3 the results of the RVE size estimation methods from both DIC and CT data are presented and compared.

Finally, in Section 3.4 the inverse calibration method is applied, and the results are presented and compared to experiments.

3.1. Microstructure reconstruction

The parameters of the VGDefX algorithm used to detect porosity in the scanned region are reported in Table 1.

The result is a pore probability map with voxel values ranging from 0 to 100. The threshold t_p used to binarize the map and identify the void inside the specimen that affects the porosity volume fraction as described in Fig. 4.

After having analyzed the morphology of the voids at different t_p, a threshold value of 10%, yielding a 4.6% porosity volume fraction, has

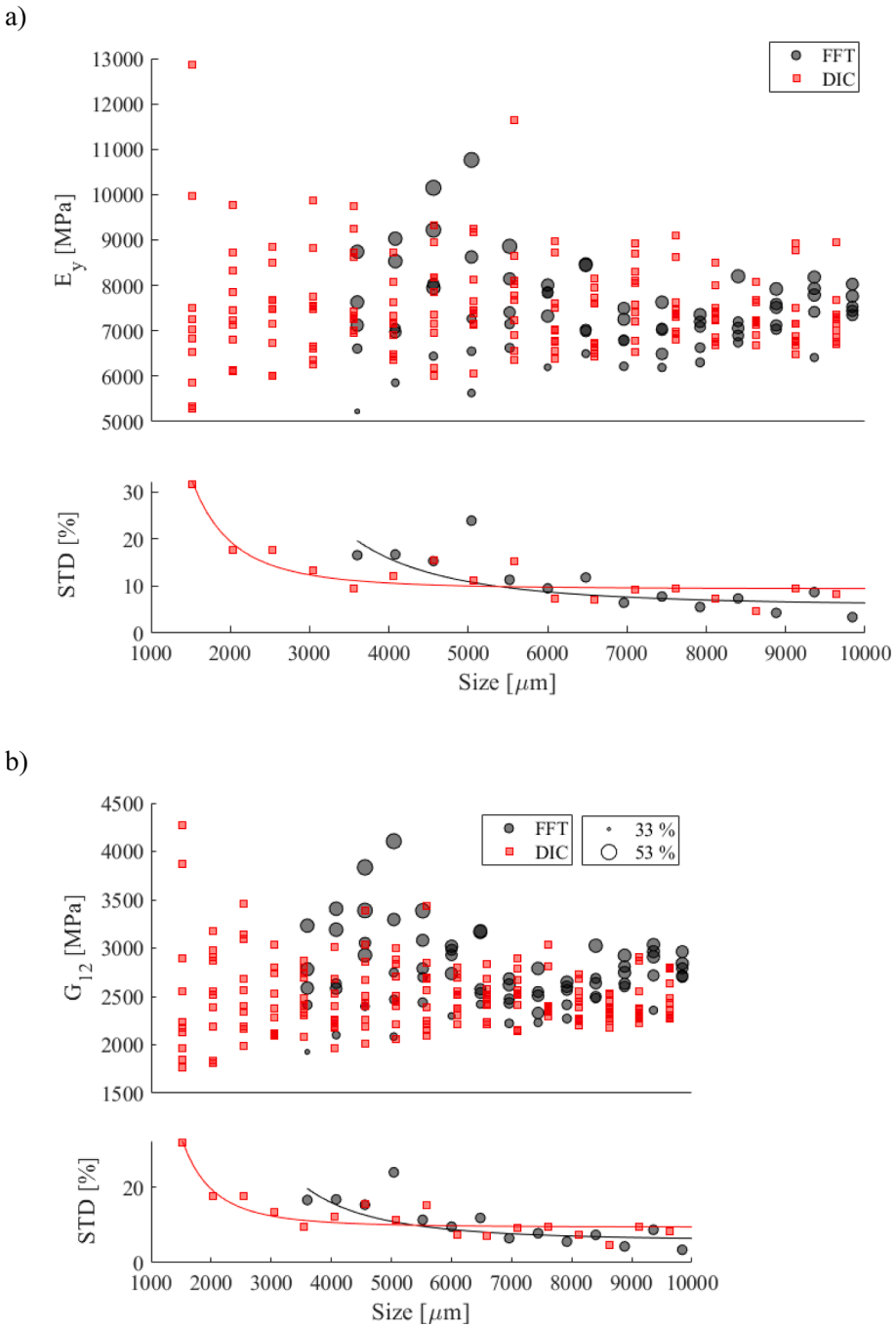

Fig. 14. Comparison of the mean value and standard deviation of the transverse Young's modulus E_{22} (a) and in-plane shear modulus G_{12} computed from FFT on CT reconstruction and DIC.

been selected since the resultant shape and orientation correspond to what was observed with the microscope. The voxels labelled as pores have been clustered with a density-based algorithm with a scanning distance of 190 μm and a minimum of 10 voxels per cluster, yielding approximately 370 clusters representing the material defects (see Fig. 3). For each defect, a sphericity index Φ has been computed, being Φ the ratio between the surface area of an equal-volume sphere and the defect surface area (A) in Eq. (8):

$$\Phi = \frac{\pi^{\frac{1}{3}}(6V)^{\frac{2}{3}}}{A} \tag{8}$$

Fig. 5 reports the sphericity and the main diameter of the segmented defects, revealing the presence of three distinguishable categories:

- Small voids with a spherical shape, whose typical shapes are sketched at the top left of Fig. 5: most probably due to trapped air in the manufacturing stage.
- Fibre-oriented defects with elliptical shapes, whose typical shapes are sketched at the top centre of Fig. 5: defects are aligned to the fibre direction and contiguous to the tows.
- Interacting defects, whose typical shapes are sketched at the top right of Fig. 5: defects made of two distinguishable defects that merged into a larger one with a distorted shape.

The categorized defects are reported in Fig. 6 and their position inside the specimen is highlighted to show the alignment of the defects to the fibre direction.

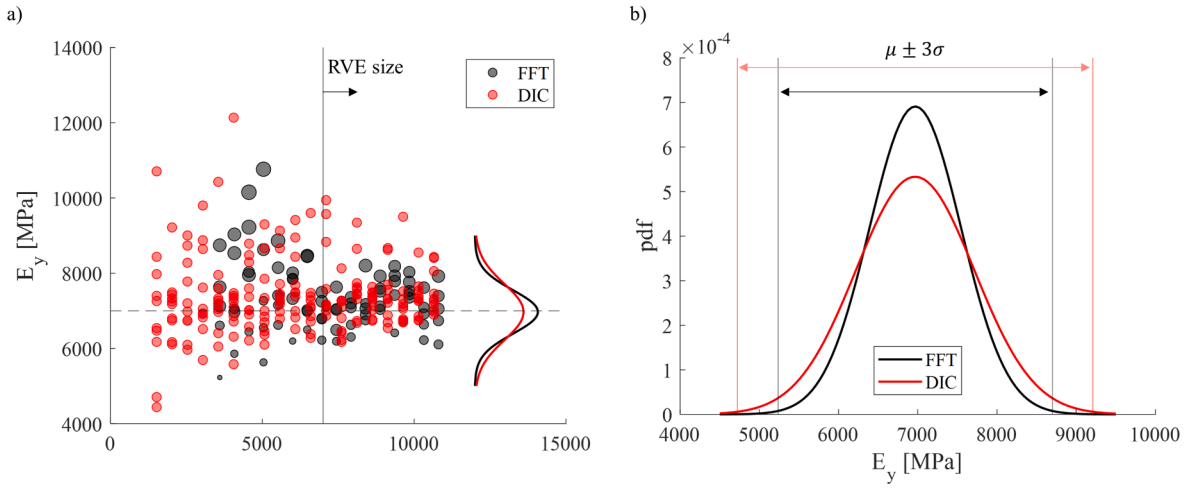

Fig. 15. A) the homogenised composite modulus extracted from the dic data is compared with the one computed with the fft model on the experimental microstructures. the fitted distributions of the modulus computed on volumes with size equal or higher to 7 mm (i.e., the RVE size) are indicatively reported on the right side of the graph, while b) shows a magnification of the normal distributions where the ± 3σ interval is reported.

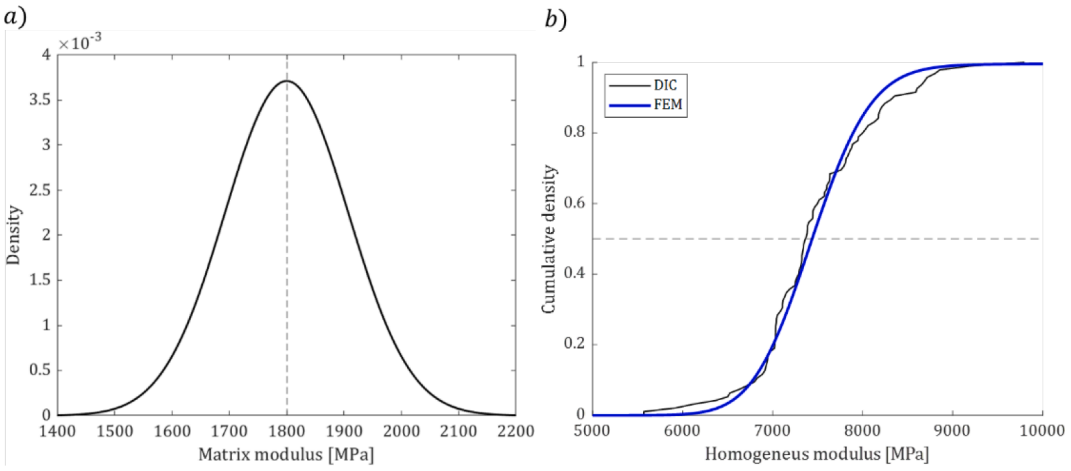

Fig. 16. A) calibrated probability density function distribution of the matrix young's modulus. b)Cdf of empirical composite modulus measurements from DIC and of SVE compared.

The irregular shape of the tows has been analysed following the same approach used for the void segmentation, applying the density-based spatial clustering technique on the voxels labelled as fibre bundles. The reconstructed fibre bundles present geometrical irregularities both in terms of alignment and size. Fig. 7a shows a slice of the reconstructed volume where the waviness of the fibre bundles can be observed. The variation of the main diameter is reported for two different tows, 1.8 mm and 2.2 mm respectively.

In the proposed approach, the variation of the fibre bundle geometry is accounted for by directly extracting the mesh of the RVE from the reconstructed structure of the composite at the mesoscale level. The effect of the bundle waviness and size on the composite stiffness is thus obtained from the experimental reconstruction, following a data-driven fashion rather than modelling its variability into an artificially generated RVE.

3.2. RVE size estimation

3.2.1. RVE size estimation from FFT analysis on CT reconstructed mesh

The RVE size estimation with FFT analysis of the reconstructed mesh has been conducted by investigating the variation of the laminate elastic modulus along the y direction. The glass fibre has been modelled as isotropic with Young's modulus of 72 GPa and a Poisson's ratio of 0.2, while the initial guesses for the epoxy matrix Young's Modulus was 2 GPa with a Poisson's ratio of 0.35, as reported in the literature[47].

The initial RVE size has been set to 3.6 mm and successively increased until the standard deviation of the homogenized modulus converged to an asymptote, whose value depends on the randomness of the microstructure extracted from the CT data. To get a statistic of the homogenized moduli, five FFT simulations have been performed for each candidate RVE, by sampling a sub-volume of the reconstructed mesh (Fig. 8).

Fig. 9 shows the results of the RVE size analysis, where it is visible the convergence of the E_{22} at a mean value of 7.6 GPa for 7 mm RVE size, where the standard deviation is approximately 5% of the mean value.

The effect of defects on the RVE response has been studied by computing the response of reconstructed microstructures where voids have not been considered, and matrix material has replaced them. The results reported in Fig. 10 show that the defects induce a larger scatter in the material response since the randomness of the material microstructure not only depends on the fibre arrangement (bundles shape, bundles alignment, matrix-rich zones) but also on the presence of defects that significantly affect the mechanical response. More specifically, it can be observed that the homogenized modulus of the defect-free material converges to a 10% higher mean value, as expected.

Since the proposed analysis investigates the elastic response of the

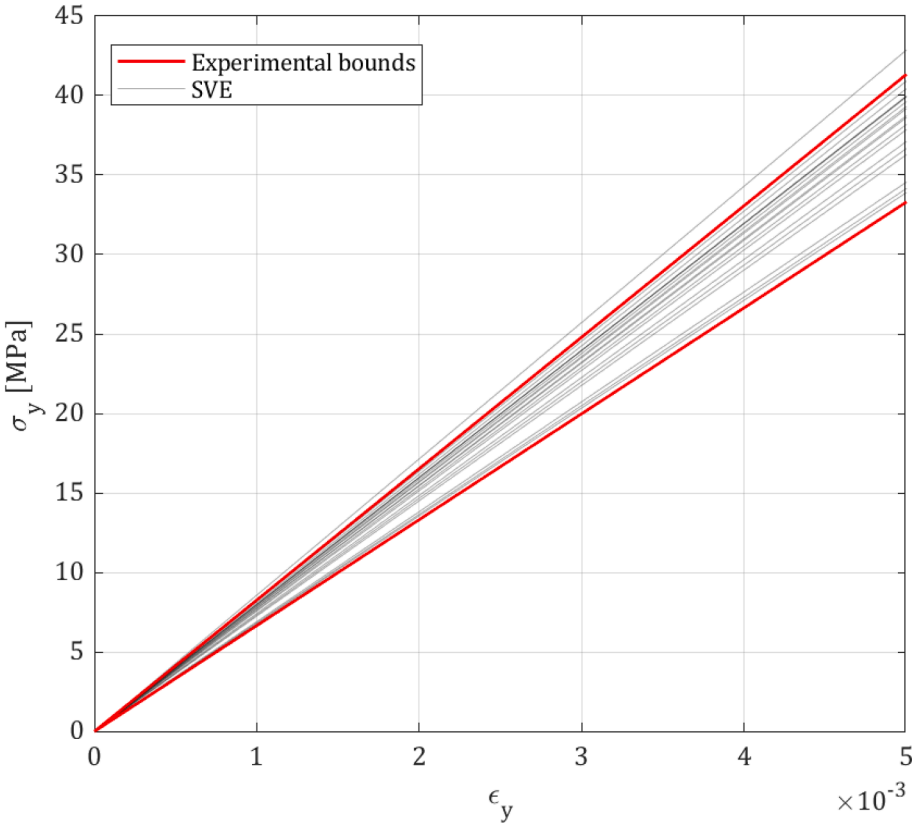

Fig. 17. Comparison between experimental curves computed from DIC maps (only upper and lower bounds are shown) and SVE results with calibrated parameters.

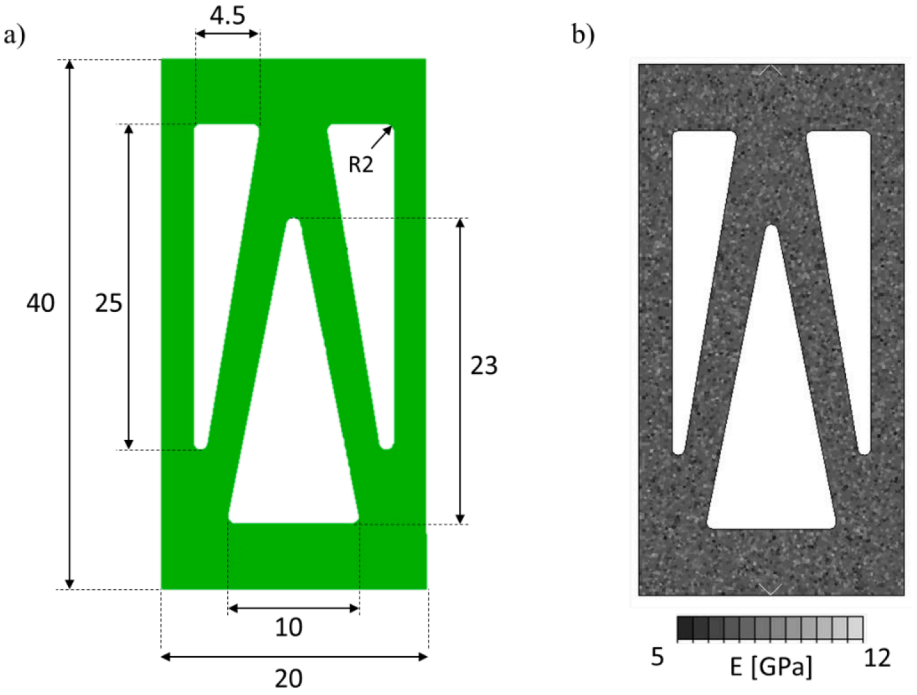

Fig. 18. A) the geometry of the virtually tested structure. b) the elastic modulus map assigned to the part with the sv-ms approach.

composite at different scales, the absence of any plasticity at the mesoscale (i.e., micro-plasticity) has been verified by analysing the equivalent Von Mises stress computed at the matrix voxels with the FFT calculations. Fig. 11 shows the equivalent stress of the matrix voxel values of each FFT simulation computed over different RVEs. The histograms contain all the computed values, whose distribution has been fitted with a logarithmic normal pdf, with a mean of 1.03 log(MPa) and a deviation of 0.47 log(MPa).

The distribution of the equivalent stress in the matrix has been compared with the yield stress values of the epoxy matrix, which is

Table 2
SV-MS algorithm.

SV-MS algorithm
Build the FE mesh of the part
Divide the elements into ***N*** groups
for each group *i*
Sample a value of Em
Sample an SVE from the reconstructed volume
Run the FFT homogenization
Generate the ith material card
Assign the material card to the ith group elements
end for

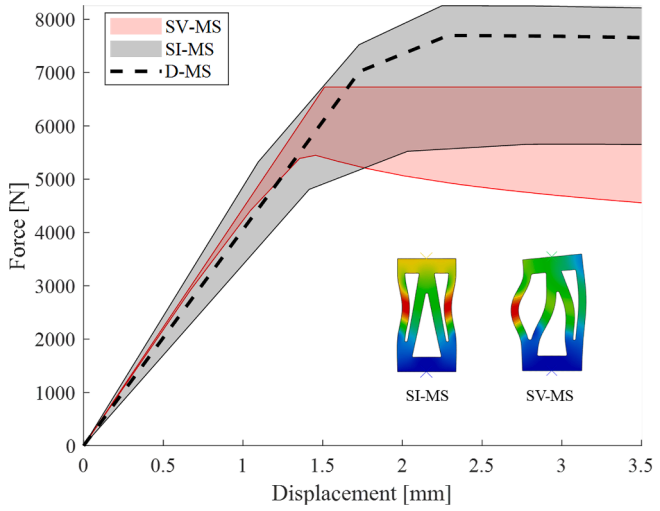

Fig. 19. Results of SV-MS and SI-MS models of skin buckling.

between 30 MPa and 50 MPa as reported in the literature [47]. It can be concluded that the average matrix response in the analysed model is within the elastic regime. The maximum values of the equivalent stress of the matrix within each RVE are reported in Fig. 11. The probability of having micro-plasticity in the extracted RVE can be described with the extreme value distribution with a mean of 15 MPa and deviation of 2.5 MPa, confirming that it is very unlikely to have plastic deformation in the analysed RVE at the defined strain level, except at lower scale where local plasticity takes place at specific inter-fibres locations.

3.2.2. *RVE size estimation from DIC measurements*

The adopted procedure for the estimation of the RVE size from the synchronized strain map and the load–displacement curve is presented in this Section 2.3.3. At each candidate size, 10 subdomains of the specimen surface have been extracted by randomly selecting the centre. Fig. 12b shows the stress–strain curve of all the extracted subdomains with distinct sizes, while the colourmap of Fig. 12a shows the strain along the y direction measured with DIC. The red dots on the specimen represent the centroids of candidate S-RVEs, with a higher density near the centreline due to the progressive reduction of the sampling sub-domain with the RVE increasing size. The red curves are related to different S-RVEs.

Applying Eqs. (1) and (2) to the extracted sub-volume, the mean and standard deviation of the transverse Young's modulus E_{22} at each size have been computed (Fig. 13).

Results show a fast convergence of the transverse Young's modulus E_{22} to the mean value of 7.2 GPa. The standard deviation for the 10 samples extracted from the strain maps converges to a value of 9% of the mean value, for an RVE size of 7 mm approximately. As it can be noticed in the upper diagram of Fig. 13, even with a larger area, the computed transverse Young's modulus has a quite large scatter arising from the DIC measures, suggesting the presence of spatially inhomogeneous properties of the material.

Table 3
FFT fixed-point iterative solution scheme.

Real space	**Fourier space**
Initialize $\boldsymbol{\varepsilon}^i(\boldsymbol{x}) = \overline{\boldsymbol{\varepsilon}}$	
$\boldsymbol{\sigma}^i(\boldsymbol{x}) = \boldsymbol{C}(\boldsymbol{x}) : \boldsymbol{\varepsilon}^i(\boldsymbol{x})$	
$\boldsymbol{\tau}(\boldsymbol{x}) = \boldsymbol{\sigma}^i(\boldsymbol{x}) - \boldsymbol{C}^0 : \boldsymbol{\varepsilon}^i(\boldsymbol{x})$	$\widehat{\boldsymbol{\tau}}^i(\boldsymbol{\xi})$
	$\widehat{\boldsymbol{\varepsilon}}^{i+1}(\boldsymbol{\xi}) = \widehat{\boldsymbol{\varepsilon}}^i - \widehat{\Gamma}(\boldsymbol{\xi}) : \widehat{\boldsymbol{\tau}}^i(\boldsymbol{\xi})$
$\boldsymbol{\varepsilon}^{i+1}(\boldsymbol{x})$	$\widehat{\boldsymbol{\varepsilon}}^{i+1}(0) = \overline{\boldsymbol{\varepsilon}}$

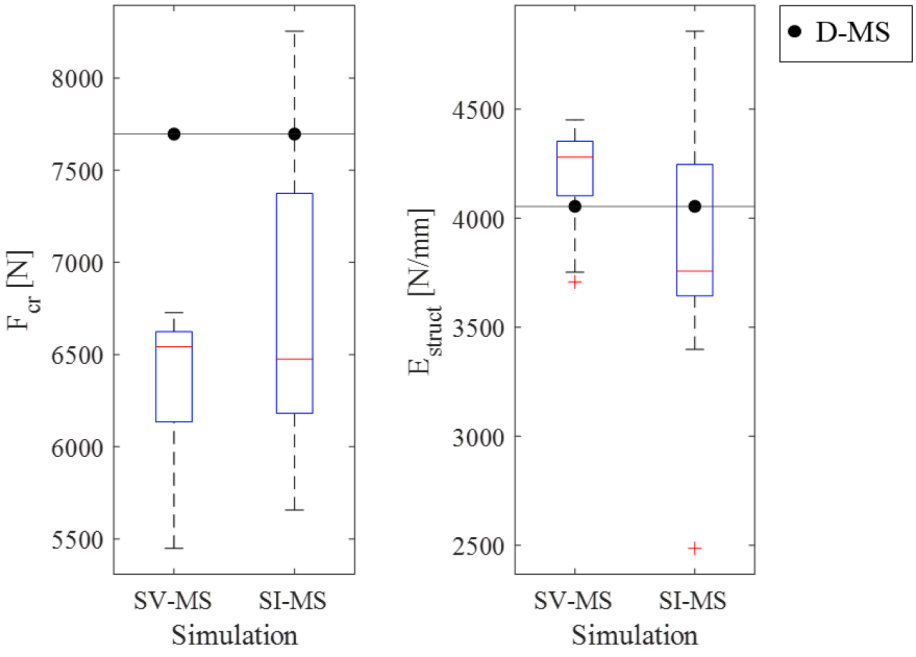

Fig. 20. Critical buckling load and structure global stiffness computed with SI-MS and SV-MS statistical models.

3.2.3. Comparison

In the diagram of Fig. 14, the results from the two presented methods are reported for values of size up to 11 mm. It is relevant to observe that the mean value of the transverse Young's modulus E_{22} computed with FFT on the reconstructed mesh converges to the homogenized value computed from the DIC maps equal to 7.3 GPa (Fig. 14a), while the in-plane shear modulus G_{12} converges to an average value of 2.5 GPa (Fig. 14b). The RVE size extracted from the DIC analysis is between 7 and 8 mm, accordingly to what was computed with the FFT simulations. The standard deviation of the homogenized elastic modulus computed with FFT approached the asymptotic deviations of 4%, while the results from the DIC maps show a larger scatter with an STD that oscillates around 9%.

The results show that the FFT model predicts a distribution of Ey with a standard deviation of 0.5 GPa, with respect to the 0.75 GPa observed experimentally Fig. 15. This 0.25 GPa difference in the standard deviation suggests that the model is not an accounting of all the stochastic phenomena that govern the elastic response of the material and raise the need for further investigation into the sources of uncertainty.

The FFT model combined with the experimental microstructure reconstruction only accounts for the defects-induced spatial variability. Indeed, the material properties have been considered spatially invariant, while recent findings demonstrated[20] the variability of the matrix properties within composites.

Therefore, both the adopted approaches are not completely satisfactory. To overcome the evidenced limitation a novel procedure has been devised. First, it is needed to assess this properties variability in the composite material, to this scope, an inverse calibration method has been applied to quantify the uncertainty imputable to the properties variability and efficiently capture it in an SVE.

3.3. SVE calibration

The inverse calibration method introduced in Section 2, requires the CDF of the homogeneous modulus probability conditioned on the matrix Young's modulus (Eq. (4)). To get this statistic, twenty values of E_m have been sampled around the expected value of 1.9 *GPa*, and the conditional homogenized modulus has been computed at each value with an FFT analysis. Using Eq. (6), the best Normal distribution parameters have been found for E_m that can capture the variability of the homogeneous modulus observed in the DIC data. It is worthy of note that the distribution of the local composite modulus, as it is well visible in the diagram of Fig. 15b, is well described by a normal distribution.

The optimization converged to a mean value of 1800 MPa with a standard deviation of 105 MPa (Fig. 16a) after 15 iterations. The loss function defined with Eq. (6) had a value of 0.29, yielding a p-value of 0.7. Fig. 16b compares the cumulative distribution function of the SVE with the one computed from the DIC, revealing a good agreement between the experimental and numerical curves.

Finally, the composite response has been calibrated using the calibrated SVE and the results with the curve extracted from the tensile test have been compared (Fig. 17).

3.4. Statistical multiscale finite element analysis

The methodology proposed in this paper wants to establish a multilength scale statistical microstructure–constitutive property relation for the design of composite parts. To demonstrate the relevance of the method, a hierarchical statistical multiscale finite element model based on the generated SVE has been developed to predict the buckling critical load of a GFRP structure. The proposed test has been virtually simulated to give a demonstration of the method's capabilities and underline the main features of the proposed work. The analysis has been performed on a structure with 2 mm thickness, whose shape is described in Fig. 18.

In the following, the results of three different models are presented:

1. Deterministic multiscale (D-MS): the homogenized properties of the material are extracted from an RVE with average properties.
2. Spatially invariant statistical multiscale (SI-MS): the homogenized properties are extracted from the SVE and applied uniformly over the domain.
3. Spatially variable statistical multiscale (SV-MS): the homogenized properties of each material point in the model are extracted from the SVE and differ over the domain.

To estimate the uncertainty of the statistical models, SI-MS and SV-MS have been run twenty times each. The SI-MS adopts the same SVE for every material point in the structure, with the matrix Young's Modulus drawn from the calibrated distribution and the microstructure randomly extracted from the scanned volume. The SV-MS model is built by sampling twenty SVE, with E_m randomly extracted from the estimated Normal distribution and the microstructure randomly sampled from the scanned volume.

The SV-MS procedure has been reported in Table 2.

The homogenization step consists of three simulations, needed to assess the homogenized elastic constants of the orthotropic stiffness matrix of the shell elements. Young's moduli along the × and y direction, together with the shear modulus and Poisson's modulus in the *xy* plane are estimated. Fig. 18b shows the map of the assigned moduli to the elements of the structure.

The diagrams in Fig. 19 report the force–displacement curves from the stochastic simulations. It can be observed that the stiffness of the structure is more variable in the SI-MS simulations, where the random value of the matrix modulus is globally assigned to every material point in the structure, leading to a larger scatter in the global response. The SV model predicts a variable global stiffness with a smaller deviation from the global stiffness computed with the D-MS. Indeed, the spatially variable method preserves the statistical distribution of the material properties over the structure domain, yielding an average result close to the mean predicted with the deterministic model (Fig. 20).

In Fig. 20, the critical load and global stiffness of each simulation are reported in a box plot. The critical load predicted with the SV-MS is always lower than the one predicted with the D-MS. In effect, it can be observed that asymmetric modes are triggered in the spatially variable model. The buckling response is indeed governed by local phenomena and more compliant SVEs concentrated in the slander regions of the structure lead to local buckling instabilities (as reported in Fig. 19). The lower critical loads are attributable to asymmetric buckling modes, that neither the D-MS nor the SI-MS can predict.

It can be concluded that the SV-MS model, by streaming the uncertainty from the microstructural to the macroscopic scale, allows for the prediction of structural behaviour triggered by the intrinsic variability of the composite material.

4. Conclusions

The article introduces novel methodologies to leverage the large data available from the most recent experimental technique for material characterization. The full field description of the microstructural geometry defined using computer tomography scans, and the full field strain response captured with the Digital Image Correlation technique feed the statistical data-driven algorithm, that links the microstructural variability and its intrinsic defectiveness with the uncertainty of the mechanical response. The inverse method allows for the estimation of the microstructural material parameter and their statistic without directly measuring them. The proposed framework makes the best out of the available data at different length scales and gives a probabilistic model for the multiscale response of composite structures. The uncertainty is propagated from the microscale to the structure in a multiscale fashion by introducing a probabilistic multiscale model based on the SVE.

The proposed method:

- Defines the RVE (or SVE) size from the experimentally measured strain maps of DIC, showing consistency with the numerical procedure based on full field homogenization (e.g., FFT),
- Estimates the uncertainty of the material model's parameters used in the microscale representation of the heterogeneous material from the CT reconstructions of the microstructure and strain map from DIC,
- Defines an SVE used in a statistical multiscale model propagating the uncertainty from the microscale to the structural level.

To assess the method potentials, the multiscale model has been used to predict the buckling response of a GFRP structure, showing it can predict mechanical responses originating from the statistical variability of the material properties over the spatial domain. Results confirm the importance of propagating the measured microstructural uncertainties, to the structure level and predicting its effect on the mechanical response. The presented method is limited to the elastic analysis of heterogeneous materials, while future development will extend the applicability to the plastic and damage models to assess the multiscale uncertainty relation behind the elastic regime.

CRediT authorship contribution statement

A Ciampaglia: Conceptualization, Methodology, Data curation, Writing – original draft, Visualization, Investigation.

Declaration of Competing Interest

The authors declare that they have no known competing financial interests or personal relationships that could have appeared to influence the work reported in this paper.

Data availability

The data that has been used is confidential.

Acknowledgements

The author wants to thank Professor Giovanni Belingardi and Professor Davide S. Paolino from Politecnico di Torino for their continuous support and guidance throughout the project and Alessandro Benelli for his assistance with the experimental characterization.

Appendix A

Homogenization method.

A.1. Two-scale equilibrium problem.

The macroscopic response of heterogeneous materials is governed by deformation mechanisms taking place at two different scales: the microscale and the macroscale. The microscale is defined but the Representative Volume Element (RVE) which has a characteristic dimension l, while the macroscale is defined by the scale of the analysed structure L. Under the assumption of linear elasticity, the two scales can be studied separately (l≪L), and the heterogeneous response of the material can be replaced by homogenized behaviour. At the macroscale, the constitutive model of the material is given by:

$$\overline{\sigma} = \overline{C}\overline{\varepsilon}, \tag{A.1}$$

With $\overline{C}$ the elastic tensor, $\overline{\sigma}$ and $\overline{\varepsilon}$ the average stress and strain fields that comply with the microscale equilibrium are given by:

$$\begin{cases} div\sigma = 0, in\Omega, \\ \varepsilon(\mathrm{x}) = \nabla^{\mathrm{S}}(u^{*}(x)) + \overline{\varepsilon}, in\Omega, \\ \sigma(x) = C_i : \varepsilon(x), in\Omega_i, \\ \nabla^{s}(u^{*}(x)) = 0, in\Omega, \end{cases} \tag{A.2}$$

where C_i is the stiffness tensor of phase i, and $\nabla^{\mathrm{S}}(u^{*}(x))$ is the fluctuating part of the strain in the RVE, whose average should vanish over the RVE.

A.2 Fast Fourier Transform (FFT) method.

Under the assumption of periodic boundary conditions, the microscale problem can be solved using the FFT method developed by H. Moulinec and P. Suquet[48]. The method proposes an auxiliary problem to A.2, introducing a reference material with a stiffness tensor C^0 and a polarization stress field $\tau(x)$. The problem can be expressed as:

$$\begin{cases} div\sigma = 0, in\Omega, \\ \varepsilon(\mathrm{x}) = \nabla^{\mathrm{S}}(u^{*}(x)) + \overline{\varepsilon}, in\Omega, \\ \sigma(x) = C^0 : \varepsilon(x) + \tau(x), in\Omega_i, \\ \tau(x) = \left(C^i - C^0\right) : \varepsilon(x), in\Omega_i, \\ \nabla^{s}(u^{*}(x)) = 0, in\Omega. \end{cases} \tag{A.3}$$

That leads to:

$$\nabla \bullet \left(C^0 : \overline{\varepsilon}\right) + \nabla \bullet \left(C^0 : \widehat{\varepsilon}\right) + \nabla \bullet (\tau(x)) = 0, \tag{A.4}$$

giving:

$$\nabla \bullet \left(C^0 : \widehat{\varepsilon}\right) = -\nabla \bullet \tau(x), \tag{A.5}$$

The solution to this problem can be expressed by introducing the isotropic Green's operator Γ^0 based on the reference material C^0:

$$\widehat{\varepsilon}(x) = -\Gamma^0 * \tau(x), in\Omega, \tag{A.6}$$

with * indicating the convolution product. Leading to:

$$\varepsilon(x) = \overline{\varepsilon} - \Gamma^0(x) * \left(\sigma(x) - C^0 : \varepsilon(x)\right), \tag{A.7}$$

Green's function for isotropic materials with applied periodic boundary conditions in the Fourier space is given by:

$$\widehat{\Gamma}^0_{ijkl} = \frac{1}{4\mu^0|\xi|}\left(\delta_{ki}\xi_h\xi_j + \delta_{li}\xi_l\xi_i + \delta_{kj}\xi_k\xi_j + \delta_{jl}\xi_j\xi_l\right) - \frac{\lambda^0+\mu^0}{\mu^0\left(\lambda^0+2\mu^0\right)}\frac{\xi_i\xi_j\xi_k\xi_l}{|\xi|^4}, \tag{A.8}$$

where ξ is the coordinate in the Fourier space, μ^0 and λ^0 are the Lame's constants of the reference materials.

The problem can then be solved iteratively with a fixed-point solution scheme, as described in Table 3:The iteration is completed until the convergence of the strain tensor.

References

[1] Ciampaglia A, Santini A, Belingardi G. Design and analysis of automotive lightweight materials suspension based on finite element analysis. Proc Inst Mech Eng C J Mech Eng Sci 2020:095440622094745. 10.1177/0954406220947457.

[2] Yang X, Sun L, Zhang C, Li L, Dai Z, Xiong Z. Design and optimization of composite automotive hatchback using integrated material-structure-process-performance method. Appl Compos Mater 2018;25:1455–75. https://doi.org/10.1007/s10443-018-9677-1.

[3] Ciampaglia A, Fiumarella D, Boursier Niutta C, Ciardiello R, Belingardi G. Impact response of an origami-shaped composite cras hbox: experimental analysis and numerical optimization. Compos Struct 2020;256:113093. https://doi.org/10.1016/j.compstruct.2020.113093.

[4] Avalle M, Chiandussi G, Belingardi G. Design optimization by response surface methodology: application to crashworthiness design of vehicle structures n.d. 10.1007/s00158-002-0243-x.

[5] Rwawiire S, Tomkova B, Militky J, Jabbar A, Kale BM. Development of a biocomposite based on green epoxy polymer and natural cellulose fabric (bark cloth) for automotive instrument panel applications. Compos B Eng 2015;81:149–57. https://doi.org/10.1016/J.COMPOSITESB.2015.06.021.

[6] Koronis G, Silva A, Fontul M. Green composites: A review of adequate materials for automotive applications. Compos B Eng 2013;44:120–7. https://doi.org/10.1016/J.COMPOSITESB.2012.07.004.

[7] Gong Y, Yang ZG. Fracture failure analysis of automotive accelerator pedal arms with polymer matrix composite material. Compos B Eng 2013;53:103–11. https://doi.org/10.1016/J.COMPOSITESB.2013.04.047.

[8] Saenz-Dominguez I, Tena I, Esnaola A, Sarrionandia M, Torre J, Aurrekoetxea J. Design and characterisation of cellular composite structures for automotive crash-boxes manufactured by out of die ultraviolet cured pultrusion. Compos B Eng 2019;160:217–24. https://doi.org/10.1016/J.COMPOSITESB.2018.10.046.

[9] Kim DH, Choi DH, Kim HS. Design optimization of a carbon fiber reinforced composite automotive lower arm. Compos B Eng 2014;58:400–7. https://doi.org/10.1016/J.COMPOSITESB.2013.10.067.

[10] Khatkar V, Behera BK, Manjunath RN. Textile structural composites for automotive leaf spring application. Compos B Eng 2020;182:107662. https://doi.org/10.1016/J.COMPOSITESB.2019.107662.

[11] Hiremath N, Young S, Ghossein H, Penumadu D, Vaidya U, Theodore M. Low cost textile-grade carbon-fiber epoxy composites for automotive and wind energy applications. Compos B Eng 2020;198:108156. https://doi.org/10.1016/J.COMPOSITESB.2020.108156.

[12] Ye J, Chu C, Cai H, Hou X, Shi B, Tian S, et al. A multi-scale model for studying failure mechanisms of composite wind turbine blades. Compos Struct 2019;212:220–9. https://doi.org/10.1016/J.COMPSTRUCT.2019.01.031.

[13] Shah DU, Schubel PJ, Clifford MJ. Can flax replace E-glass in structural composites? a small wind turbine blade case study. Compos B Eng 2013;52:172–81. https://doi.org/10.1016/J.COMPOSITESB.2013.04.027.

[14] Belfkira Z, Mounir H, el Marjani A. Structural optimization of a horizontal axis wind turbine blade made from new hybrid composites with kenaf fibers. Compos Struct 2021;260:113252. https://doi.org/10.1016/J.COMPSTRUCT.2020.113252.

[15] McVeigh C, Vernerey F, Liu WK, Cate BL. Multiresolution analysis for material design. Comput Methods Appl Mech Eng 2006;195:5053–76. https://doi.org/10.1016/J.CMA.2005.07.027.

[16] Patel DK, Waas AM. Multiscale analysis of notched fiber reinforced laminates. Compos B Eng 2019;173:106986. https://doi.org/10.1016/J.COMPOSITESB.2019.106986.

[17] Shah SZH, Megat-Yusoff PSM, Karuppanan S, Choudhry RS, Sajid Z. Multiscale damage modelling of 3D woven composites under static and impact loads. Compos Part A Appl Sci Manuf 2021;151:106659. https://doi.org/10.1016/J.COMPOSITESA.2021.106659.

[18] Koohbor B, Ravindran S, Kidane A. A multiscale experimental approach for correlating global and local deformation response in woven composites. Compos Struct 2018;194:328–34. https://doi.org/10.1016/J.COMPSTRUCT.2018.04.016.

[19] Tikarrouchine E, Benaarbia A, Chatzigeorgiou G, Meraghni F. Non-linear FE2 multiscale simulation of damage, micro and macroscopic strains in polyamide 66-woven composite structures: analysis and experimental validation. Compos Struct 2021;255:112926. https://doi.org/10.1016/J.COMPSTRUCT.2020.112926.

[20] Chevalier J, Camanho PP, Lani F, Pardoen T. Multi-scale characterization and modelling of the transverse compression response of unidirectional carbon fiber reinforced epoxy 2018. https://doi.org/10.1016/j.compstruct.2018.10.076.

[21] Fish J. Practical multiscaling 2013;3.

[22] Sun CT, Vaidya RS. Prediction of composite properties from a representative volume element. Compos Sci Technol 1996;56:171–9. https://doi.org/10.1016/0266-3538(95)00141-7.

[23] Cule D, Torquato S. Generating random media from limited microstructural information via stochastic optimization. J Appl Phys 1999;86:3428. https://doi.org/10.1063/1.371225.

[24] Li M, Ghosh S, Richmond O, Weiland H, Rouns TN. Three dimensional characterization and modeling of particle reinforced metal matrix composites: part I: quantitative description of microstructural morphology. Mater Sci Eng: A 1999;265:153–73. https://doi.org/10.1016/S0921-5093(98)01132-0.

[25] Sankaran S, Zabaras N. Computing property variability of polycrystals induced by grain size and orientation uncertainties. Acta Mater 2007;55:2279–90. https://doi.org/10.1016/J.ACTAMAT.2006.11.025.

[26] Al-Ostaz Anipindi Diwakar AE Khalid I Alzebdeh AA. Statistical model for characterizing random microstructure of inclusion-matrix composites n.d. 10.1007/s10853-006-1117-1.

[27] Kamgaing Somoh G, ben Toumi R, Renard J, Monin M. Statistical approach of elastic properties of continuous fiber composite. Compos Struct 2015;119:287–97. 10.1016/J.COMPSTRUCT.2014.08.039.

[28] Lim HJ, Choi H, Yun GJ. Multiscale failure and damage analysis of sheet molding compound (SMC) composites using Micro-CT image-based reconstruction model. Compos B Eng 2022;231:109593. https://doi.org/10.1016/J.COMPOSITESB.2021.109593.

[29] Huang T, Gao J, Sun Q, Zeng D, Su X, Kam Liu W, et al. Stochastic nonlinear analysis of unidirectional fiber composites using image-based microstructural uncertainty quantification. Compos Struct 2021;260:113470. https://doi.org/10.1016/j.compstruct.2020.113470.

[30] Yin X, Chen W, To A, McVeigh C, Liu WK. Statistical volume element method for predicting microstructure–constitutive property relations. Comput Methods Appl Mech Eng 2008;197:3516–29. https://doi.org/10.1016/J.CMA.2008.01.008.

[31] Li YY, Cui JZ. The multi-scale computational method for the mechanics parameters of the materials with random distribution of multi-scale grains. Compos Sci Technol 2005;65:1447–58. https://doi.org/10.1016/J.COMPSCITECH.2004.12.016.

[32] Wang B, Fang G, Wang H, Liang J, Dai F, Meng S. Uncertainty modelling and multiscale simulation of woven composite twisted structure. Compos Sci Technol 2022;217:109118. https://doi.org/10.1016/J.COMPSCITECH.2021.109118.

[33] Tao W, Zhu P, Xu C, Liu Z. Uncertainty quantification of mechanical properties for three-dimensional orthogonal woven composites. Part II: Multiscale simulation Compos Struct 2020;235:111764. https://doi.org/10.1016/J.COMPSTRUCT.2019.111764.

[34] Pingaro M, de Bellis ML, Reccia E, Trovalusci P, Sadowski T. Fast statistical homogenization procedure for estimation of effective properties of ceramic matrix composites (CMC) with random microstructure. Compos Struct 2023;304:116265. https://doi.org/10.1016/J.COMPSTRUCT.2022.116265.

[35] Vinot M, Liebold C, Usta T, Holzapfel M, Toso N, Voggenreiter H. Stochastic modelling of continuous glass-fibre reinforced plastics–considering material uncertainty in microscale simulations. J Compos Mater 2022:1–13. https://doi.org/10.1177/00219983221139790/ASSET/IMAGES/LARGE/10.1177_00219983221139790-FIG14.JPEG.

[36] Gao SL, Mäder E. Characterisation of interphase nanoscale property variations in glass fibre reinforced polypropylene and epoxy resin composites. Compos Part A Appl Sci Manuf 2002;33:559–76. https://doi.org/10.1016/S1359-835X(01)00134-8.

[37] Vanlandingham MR, Dagastine RR, Eduljee RF, McCullough RL, Gillespie JW. Characterization of nanoscale property variations in polymer composite systems: 1. experimental results. Compos Part A Appl Sci Manuf 1999;30:75–83. https://doi.org/10.1016/S1359-835X(98)00098-0.

[38] Hardiman M, Vaughan TJ, McCarthy CT. Fibrous composite matrix characterisation using nanoindentation: the effect of fibre constraint and the evolution from bulk to in-situ matrix properties. Compos Part A Appl Sci Manuf 2015;68:296–303. https://doi.org/10.1016/J.COMPOSITESA.2014.09.022.

[39] Bahrami A, Morelle X, Hông Minh LD, Pardoen T, Bailly C, Nysten B. Curing dependent spatial heterogeneity of mechanical response in epoxy resins revealed by atomic force microscopy. Polymer (Guildf) 2015;68:1–10. https://doi.org/10.1016/J.POLYMER.2015.04.084.

[40] Koohbor B, Ravindran S, Kidane A. Experimental determination of Representative Volume Element (RVE) size in woven composites. Opt Lasers Eng 2017;90:59–71. https://doi.org/10.1016/j.optlaseng.2016.10.001.

[41] Koohbor B, Montgomery CB, Sottos NR. Identification of RVE length scale in fiber composites via combined optical and SEM digital image correlation. Compos Sci Technol 2022;227:109613. https://doi.org/10.1016/J.COMPSCITECH.2022.109613.

[42] Massey FJ. The kolmogorov-smirnov test for goodness of Fit. Source. J Am Statistical Association 1951;46:68–78.

[43] Gusev AA. Representative volume element size for elastic composites: a numerical study. J Mech Phys Solids 1997;45:1449–59. https://doi.org/10.1016/S0022-5096(97)00016-1.
[44] Ivanov D, Ivanov S, Lomov S, Verpoest I. Strain mapping analysis of textile composites. Opt Lasers Eng 2009;47:360–70. https://doi.org/10.1016/J.OPTLASENG.2008.05.013.
[45] Ivanov DS, Lomov SV, Ivanov SG, Verpoest I. Stress distribution in outer and inner plies of textile laminates and novel boundary conditions for unit cell analysis. Compos Part A Appl Sci Manuf 2010;41:571–80. https://doi.org/10.1016/J.COMPOSITESA.2010.01.004.
[46] Byrd RH, Hribar ME, Nocedal J. An Interior Point Algorithm for Large-Scale Nonlinear Programming. Https://DoiOrg/101137/S1052623497325107 2006;9:877–900. 10.1137/S1052623497325107.
[47] Kaddour A, Hinton M. Input data for test cases used in benchmarking triaxial failure theories of composites. J Compos Mater 2012;46:2295–312. https://doi.org/10.1177/0021998312449886.
[48] Moulinec H, Suquet P. A fast numerical method for computing the linear and nonlinear mechanical properties of composites n.d.